

Weakly Supervised Estimation of Shadow Confidence Maps in Ultrasound Imaging

Qingjie Meng, Matthew Sinclair, Veronika Zimmer, Benjamin Hou, Martin Rajchl, Nicolas Toussaint, Alberto Gomez, James Housden, Jacqueline Matthew, Daniel Rueckert, Julia Schnabel, and Bernhard Kainz

Abstract—Detecting acoustic shadows in ultrasound images is important in many clinical and engineering applications. Real-time feedback of acoustic shadows can guide sonographers to a standardized diagnostic viewing plane with minimal artifacts and can provide additional information for other automatic image analysis algorithms. However, automatically detecting shadow regions is challenging because pixel-wise annotation of acoustic shadows is subjective and time consuming. In this paper we propose a weakly supervised method for automatic confidence estimation of acoustic shadow regions, which is able to generate a dense shadow-focused confidence map. During training, a multi-task module for shadow segmentation is built to learn general shadow features according based image-level annotations as well as a small number of coarse pixel-wise shadow annotations. A transfer function is then established to extend the binary shadow segmentation to a reference confidence map. In addition, a confidence estimation network is proposed to learn the mapping between input images and the reference confidence maps. This confidence estimation network is able to predict shadow confidence maps directly from input images during inference. We evaluate DICE, soft DICE, recall, precision, mean squared error and inter-class correlation to verify the effectiveness of our method. Our method outperforms the state-of-the-art qualitatively and quantitatively. We further demonstrate the applicability of our method by integrating shadow confidence maps into tasks such as ultrasound image classification, multi-view image fusion and automated biometric measurements.¹

I. INTRODUCTION

ULTRASOUND (US) imaging is a medical imaging technique based on reflection and scattering of high-frequency sound in tissues. Compared with other imaging techniques (e.g. Magnetic Resonance Imaging (MRI) and Computed Tomography (CT)), US imaging has various advantages including portability, low cost, high temporal resolution, no radiation exposure and real-time imaging capability. With these advantages, US is an important medical imaging modality that is utilized to examine a range of anatomical structures in both adults and fetuses. In most countries, US imaging is an essential part of clinical routine for pregnancy examination between 18 and 22 weeks of gestation [28].

Although US imaging is capable of providing real-time images of anatomy, diagnostic accuracy is limited by low intensity contrast and challenging interpretation, which are caused by artifacts such as noise [1], distortions [33] and acoustic shadows [12]. These artifacts are unavoidable in clinical practice due to the low energies used and the physical

nature of sound wave propagation in human tissues. Better hardware and advanced image reconstruction algorithms have been developed to reduce speckle noise [9, 10]. Prior anatomical expertise [20] and extensive sonographer training are the only way to handle distortions and shadows to date.

Sound-opaque occluders, including bones and calcified tissues, block the propagation of sound waves by strongly absorbing or reflecting sound waves during scanning, so that the regions behind these sound-opaque occluders return little to no reflections to the US transducer. Thus these areas have low intensity but very high acoustic impedance gradients at the boundaries. Reducing acoustic shadows and correct interpretation of images containing shadows rely heavily on sonographer experience. Experienced sonographers avoid shadows by moving the probe to a more preferable viewing direction during scanning or, if no shadow-free viewing direction can be found, a mental map is compounded with iterative acquisitions from different orientations.

With less anatomical information in shadow regions, especially when shadows cut through the anatomy of interest, images containing strong shadows can be problematic for automatic real-time image analysis methods such as biometric measurements [31], anatomy segmentation [5] and US image classification [3]. Moreover, the shortage of experienced sonographers [8] exacerbates the challenges of accurate US image-based screening and diagnostics. Therefore, shadow-aware US image analysis is greatly needed and would be beneficial both for engineers who work on medical image analysis, as well as for sonographers in clinical practice.

A. Contribution

We propose a novel method based on convolutional neural networks (CNNs) to automatically estimate pixel-wise confidence maps of acoustic shadows in 2D US images. Our method learns an initial latent space of shadow regions from images with image-level labels (“has shadow” and “shadow-free”) of multiple classes of anatomy. The basic latent space is generalized by learning from few images of a single anatomy (fetal brain) with coarse pixel-wise shadow annotations (approximately 10% of the images with image-level labels). The resulting latent space is then refined by learning shadow intensity distribution using the above fetal brain images so that the latent space is suitable for confidence estimation of shadow regions. By using information about shadow intensity distributions, our method can detect more shadow regions than the coarse manual segmentation, especially relatively weak shadow regions.

¹This work has been submitted to the IEEE for possible publication. Copyright may be transferred without notice, after which this version may no longer be accessible.

The proposed training process is able to build a direct mapping between input images and the corresponding shadow confidence maps in any given anatomy, which allows real-time application through direct inference.

In contrast to our preliminary work [21], which uses separate, heuristically linked components, here we establish a pipeline to make full use of existing data sets and annotations. During inference our method can predict both a binary shadow segmentation and a dense shadow-focused confidence map. The shadow segmentation is not limited by hyperparameters such as thresholds in [21], and the segmentation accuracy as well as probabilistic shadow confidence maps are greatly improved compared to the state-of-the-art (shown in Fig. 7).

We have demonstrated in [21] that shadow confidence maps can improve the performance of an automatic biometric measurement task. In this study, we further evaluate the usefulness of the shadow confidence estimation for other automatic image analysis algorithms such as an US image classification task and a multi-view image fusion task.

B. Related work

Automatic US shadow detection: Acoustic shadows have a significant impact on US image quality, and thus a serious effect on robustness and accuracy of image processing methods. In clinical literature, US artifacts including shadows have been well studied and reviewed [6, 18, 23]. However, the shadow problem is not well covered in automated US image analysis literature. Anatomically estimating acoustic shadow has rarely been the focus within the medical image analysis community as it is a challenging task.

Identifying shadow regions in US images has been utilized as a preprocessing step for extracting valid image content and improving image analysis accuracy in some applications. [26] has identified shadow regions by thresholding the accumulated intensity along each scanning beam line. Afterwards, these shadow regions have been masked out from US images for an US to magnetic resonance (MR) hepatic image registration. Instead of excluding shadow regions, [16] focused on accurate attenuation estimation, and aimed to use attenuation properties for determination of the anatomical properties which can help diagnose diseases. [16] proposed a hybrid attenuation estimation method that combines spectral difference and spectral shift methods to reduce the influence of local spectral noise and backscatter variations in Radio Frequency (RF) US data. To detect shadow regions in B-Mode scans directly and automatically, [14] have introduced the probe's geometric information and statistically modelled the US B-Mode cone. Compared with previous statistical shadow detection methods such as [26], this method can automatically estimate the probe's geometry as well as other hyperparameters, and has shown improvements in 3D reconstruction, registration and tracking. However, this method can only detect a subset of 'deep' acoustic shadows because of the probe geometry-dependant sampling strategy.

To improve the accuracy of US attenuation estimation and shadow detection, [15] proposed a more general solution using the Random Walks (RW) algorithm to predict the per-pixel

confidence of US images. In [15], confidence maps represent the uncertainty of US images resulting from shadows, and thus, show the acoustic shadow regions. The confidence maps obtained by this work can improve the accuracy of US image processing tasks, such as intensity-based US image reconstruction and multi-modal registration. However, such confidence maps are sensitive to US transducer settings and limited by the US formation process. [17] has further extended the RW method to generate distribution-based confidence maps and applied it to RF US data. This method is more robust since the confidence prediction is no longer intensity-based.

Some studies have utilized acoustic shadow detection as additional information in their pipeline for other US image processing tasks. [7] combined acoustic shadow detection for the characterization of dense calcium tissue in intravascular US virtual histology, and [5] automatically and simultaneously segment vertebrae, spinous process and acoustic shadow in US images for a better assessment of scoliosis progression. In these applications, acoustic shadow detection is task-specific, and is mainly based on heuristic image intensity features as well as special anatomical constraints.

The aforementioned literature relies heavily on manually selected relevant features, intensity information or a probe-specific US formation process. With the advances in deep learning, US image analysis algorithms have gained better semantic image interpretation abilities. However, current deep learning segmentation methods require a large amount of pixel-wise, manually labelled ground truth images. This is challenging in the US imaging domain because of (a) a lack of experienced annotators and (b) weakly defined structural features that cause a high inter-observer variability.

Weakly supervised image segmentation: Weakly supervised automatic detection of class differences has been explored in other imaging domains (e.g. MRI). For example, [4] proposed to use generative adversarial network (GAN) to highlight class differences only from image-level labels (Alzheimer's disease or healthy). We used a similar idea in [21] and initialized potential shadow areas based on saliency maps [32] from a classification task between images containing shadow and those without shadow. Inspired by recent weakly supervised deep learning methods that have drastically improved semantic image analysis [19, 27, 36] and to overcome the limitations of [21], we develop a confidence estimation algorithm that takes advantages of both types of weak labels, including image-level labels and a sparse set of coarse pixel-wise labels. Our method is able to predict dense, shadow-focused confidence maps directly from input US images in real-time.

II. METHOD

In our proposed method, a multi-task module is first trained to produce a semantic segmentation of shadow regions. In this modular, weights are shared between feature encoders of a shadow/shadow-free classification network and a shadow segmentation network. After obtaining the shadow segmentation, a transfer function is used to extend the binary mask of a predicted shadow segmentation to a confidence map based on the intensity distribution within suspected shadow regions.

This confidence map is regarded as a reference for the next confidence estimation network. Lastly, a confidence estimation network is trained to learn the mapping between the input shadow-containing US images and the corresponding reference confidence maps. The outline for the training process of our method is shown in Fig. 1. During inference, we only use the confidence estimation network to predict a dense, shadow confidence map directly from the input image. Additionally, we integrate attention mechanisms [29] into our method to enhance the shadow features extracted by the networks.

A. Multi-task Module

We propose a multi-task module to extract generalized shadow features for a large range of shadow types under limited weak manual annotations. Since shadow regions have different shapes, various intensity distributions and uncertain edges, pixel-wise annotation of shadow regions relies heavily on annotator's experience and is time consuming. This generally results in manual annotations of limited quantity and quality. Compared with the pixel-wise shadow annotation, image-level labels ("has shadow" and "shadow-free" in our case) are easier to obtain, and shadow images with image-level labels can contain a larger variety of shadow types. Therefore, we use a multi-task module that combines unreliable pixel-wise annotations and image-level labels as weak annotations. The proposed multi-task module contains two tasks, (1) shadow/shadow-free classification using image-level labels, and (2) shadow segmentation that uses few coarse pixel-wise manual annotations (10% of the image-level labels). Shadow features are generalized in this module by sharing weights between feature encoders of both tasks. By sharing weights, shadow features can be extracted during simple shadow/shadow-free classification and subsequently optimized for the more challenging shadow segmentation task. In our case, specifically, shadow features extracted by the classification network cover various shadow types in a range of anatomical structures, and these shadow features become suitable for the shadow segmentation after being optimized by a shadow segmentation network.

Network Architecture: We build two sub-networks from residual-blocks [13] as shown in Fig. 2. The first and initially trained network is a shadow/shadow-free classification network that learns to distinguish images containing shadows from shadow-free images, and thus learns the defining features of acoustic shadow. This classification network consists of a feature encoder followed by a global average pooling layer. The feature encoder uses six residual-blocks (Fig. 2) to extract shadow features that distinguish shadow-containing images in the classifier. We refer to $l = 1$ as the label of the shadow-containing class and $l = 0$ as the label of the shadow-free class. Image set $X^C = \{x_1^C, x_2^C, \dots, x_K^C\}$ and their corresponding labels $L = \{l_1, l_2, \dots, l_K\}$ s.t. $l_i \in \{0, 1\}$ are used to train the feature encoder as well as the global average pooling layer. We use softmax cross entropy loss as the cost function L_C between the predicted labels and the true labels.

Representative shadow features extracted by the feature encoder of the shadow/shadow-free classification network are

then optimized by the shadow segmentation network with a limited number of densely segmented US images. The feature encoder of the segmentation network has the same architecture as the classification network. By sharing their weights, the feature encoders in both networks are fine-tuned so that the extracted shadow features are suitable for the segmentation in addition to classification. The decoder of the segmentation network is symmetrical to the feature encoder. Feature layers from the feature encoder are concatenated to the corresponding layers in the decoder by skip connections. Here, we denote the image set used to train the shadow segmentation with $X^S = \{x_1^S, x_2^S, \dots, x_M^S\}$ and the corresponding pixel-wise manual segmentation with $Y^S = \{y_1^S, y_2^S, \dots, y_M^S\}$. The shadow segmentation provides a pixel-wise binary prediction $\hat{Y}^S = \{\hat{y}_1^S, \hat{y}_2^S, \dots, \hat{y}_M^S\}$ for shadow regions and the cost function is the softmax cross entropy between \hat{Y}^S and Y^S .

B. Transfer Function

Binary masks lack information about inherent uncertainties at the boundaries of shadow regions. Therefore, we use a transfer function to extend the binary segmentation prediction to a confidence map, which is more appropriate to describe shadow regions. The main task of the transfer function is to learn the intensity distribution of shadow regions so that to estimate confidence of pixels in false positive (FP) regions of the predicted binary shadow segmentation. This transfer function is built and only used during training to provide reference confidence maps for the confidence estimation network.

When comparing the manual segmentation y^S and the predicted segmentation \hat{y}^S of shadow regions in image x , we define the true positive (TP) regions x_{TP} as shadow regions with the full confidence, $C_{x_{ij}} = 1, x_{ij} \in x_{TP}$. Here, $C_{x_{ij}}$ refers to the confidence of pixel x_{ij} being shadow.

For each pixel x_{ij} in the FP regions (x_{FP}), the confidence of belonging to a shadow region is computed by a transfer function $T(x_{ij} \mid x_{ij} \in x_{FP})$ based on the intensity of the pixel ($I_{x_{ij}}$) and the mean intensity of x_{TP} (I_{mean}). I_{mean} is defined in Eq. 1. With weak signals in the shadow regions, the average intensity of shadow pixels is lower than the maximum intensity ($I_{max} = \max(x)$) but not lower than the minimum intensity ($I_{min} = \min(x)$), that is $I_{mean} \in [I_{min}, I_{max}]$.

$$I_{mean} = \begin{cases} \text{mean}(y^S \cap \hat{y}^S) & y^S \cap \hat{y}^S \neq \emptyset, \\ \text{mean}(y^S) & y^S \cap \hat{y}^S = \emptyset, \end{cases} \quad (1)$$

The transfer function $T(\cdot)$ computing $C_{x_{ij}}$ for pixels in x_{FP} is defined according to the range of I_{mean} . For $I_{mean} \in (I_{min}, I_{max})$, $T(\cdot)$ is shown in Eq. 2. For $I_{mean} = I_{min}$, $T(x_{ij} \mid x_{ij} \in x_{FP}) = 1$ if $I_{x_{ij}} = I_{mean}$, otherwise $T(x_{ij} \mid x_{ij} \in x_{FP}) = \frac{I_{x_{ij}} - I_{mean}}{I_{max} - I_{mean}}$.

$$T(x_{ij} \mid x_{ij} \in x_{FP}) = \begin{cases} \frac{I_{x_{ij}} - I_{min}}{I_{mean} - I_{min}}, & I_{min} \leq I_{x_{ij}} < I_{mean}, \\ \frac{I_{max} - I_{x_{ij}}}{I_{max} - I_{mean}}, & I_{mean} < I_{x_{ij}} \leq I_{max}, \\ 1, & I_{x_{ij}} = I_{mean}, \end{cases} \quad (2)$$

After using the transfer function, the binary map of the predicted segmentation y^S is extended to a confidence map

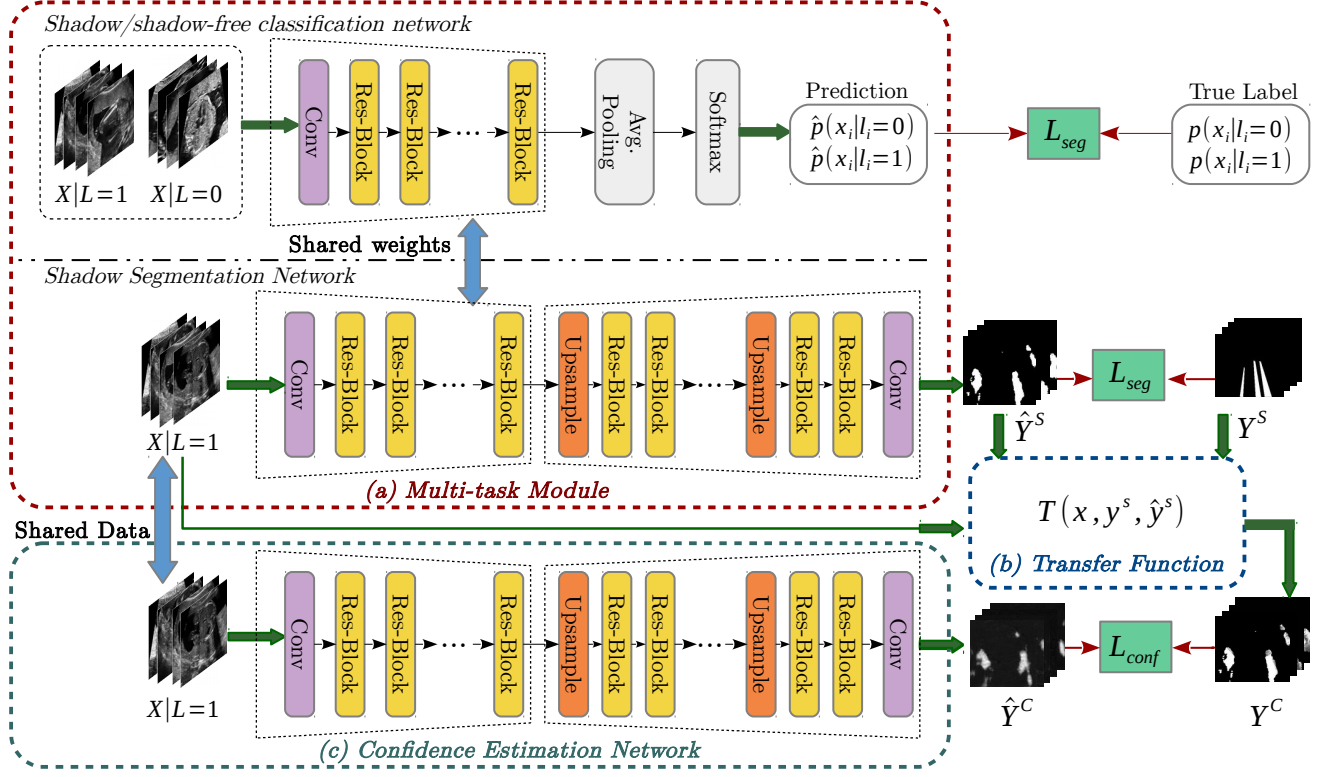


Fig. 1: Training framework of the proposed method. (a) The multi-task module containing a shadow/shadow-free classification network and a shadow segmentation network. (b) The transfer function that expands a binary mask to a reference confidence map. (c) The confidence estimation network which establishes direct mapping between input images and confidence maps.

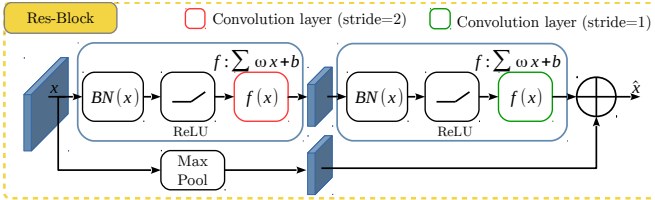


Fig. 2: The architecture of the residual-block. $BN(x)$ refers to a batch normalization layer and $f(x)$ is a convolutional layer.

y^C . y^C acts as a reference (“ground truth”) for the training of the next confidence estimation network.

C. Confidence Estimation Network

After obtaining reference confidence maps from the predicted binary segmentation, a confidence estimation network is trained to map an image with shadows (x) to the corresponding reference confidence map (y^C). This confidence estimation network can be independently used to directly predict a dense shadow confidence map for an input image during inference.

The confidence estimation network consists of a down-sampling encoder, a symmetric up-sampling decoder, and skip connections between feature layers from the encoder and the decoder at different resolution levels. Both the encoder and the decoder are composed of six residual-blocks, which reduces the training error of using a deeper network and results in easier network optimization [13]. The cost function of the

confidence estimation network is defined as the mean squared error between the predicted confidence map \hat{Y}^C and the reference confidence map Y^C ($\mathcal{L}_{conf} = \|\hat{Y}^C - Y^C\|_2$).

D. Attention Gates

Attention gates can improve network performance for medical image analysis [24]. We integrate attention gates [29] into our approach to explore if attention mechanisms can further improve the confidence estimation of shadow regions in 2D ultrasound. Since attention mechanisms are able to highlight relevant features according to image context, these mechanisms can be used to guide the networks to focus on shadow features. In our case, we integrate a self-attention gating module as proposed in [24] into all three networks. We connect the self-attention gating modules to the feature maps before the last two down-sampling operations in the encoders of all networks. For the shadow/shadow-free classification network, the global average pooling layer is modified when adding this self-attention gating module. In detail, as shown in Fig. 3, after extracting feature maps from all resolution levels and applying the self-attention gating module to the last two resolution levels, the global average pooling layers are operated separately on the two attention-gated feature maps as well as the original last feature map to obtain three average feature maps. These three average feature maps are then concatenated, followed by a fully connected layer to compute the final classification prediction.

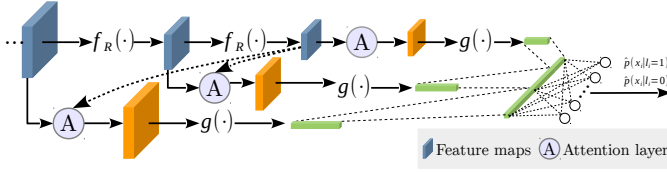


Fig. 3: The architecture of the shadow/shadow-free classification network with attention mechanism. $f_R(\cdot)$ refers to residual-blocks. $g(\cdot)$ refers to a global average pooling layer.

III. IMPLEMENTATION

All the residual-blocks used in the proposed method are implemented as proposed by [25].

We optimize the different modules separately and consecutively in three steps. First we perform approximate 70-epoch updates for the parameters of the shadow/shadow-free classification network, and then about 700-epoch for pixel-wise shadow segmentation network. After obtaining a well-trained shadow segmentation network, we train the confidence estimation network for another 700-epoch.

For all networks, we use Stochastic Gradient Descent (SGD) with momentum optimizer to update the parameters since SGD has better generalization capability than adaptive optimizer [35]. The parameters of the optimizer are $momentum = 0.9$, with a learning rate of 10^{-3} . We apply L2 regularization to all weights during training to help prevent network over-fitting. The scale of the regularizer is set as 10^{-5} . The training batch size is 25 and our networks are trained on a Nvidia Titan X GPU with 12 GB of memory.

IV. EVALUATIONS

The proposed method is trained and evaluated using two data sets, (1) a multi-class data set consisting of 13 categories of 2D US fetal anatomy with image-level label (“has shadow” or “shadow-free”), and (2) a single-class data set containing 2D US fetal brain with coarse pixel-wise manual segmentation of shadow regions. In the first data set we use 88% of the data for training, 11% for validation and the remaining for testing, while in the second data set we use 78% of the data for training, 8% for validation and 14% for testing.

To verify the effectiveness of the proposed method and the importance of the shadow/shadow-free classification network in the multi-task module, we compare the variants of our method to a baseline which only contains a shadow segmentation network and a confidence estimation network. The baseline is described in detail in Part.B of this section.

We use standard measurements such as Dice coefficient (DICE) [11], recall, precision and Mean Squared Error (MSE) for shadow segmentation evaluation, and use the Interclass Correlation (ICC) [30] as well as soft DICE [2] for confidence estimation evaluation. In order to verify the performance of our method, we also compute quantitative measurements between the chosen manual annotation (weak ground truth) and another manual annotation from a different annotator to show the human performance for the shadow detection task. Lastly, we show the practical benefits of shadow confidence maps for different applications such as a standard plane classification task,

an image fusion task from multiple views and a segmentation task for automatic biometric measurements.

A. Data Sets

Multi-class data set: This data set consists of $\sim 8.5k$ 2D fetal US images sampled from 13 different anatomical standard plane locations as defined in the UK FASP handbook [22]. These images have been sampled from 2694 2D ultrasound examinations from volunteers with gestational ages between 18 – 22 weeks. Eight different ultrasound systems of identical make and model (GE Voluson E8) were used for the acquisitions. The images have been classified by expert observers as containing strong shadow, being clear, or being corrupted, e.g. poor tissue contact caused by lacking acoustic impedance gel. Corrupted images ($< 3\%$) have been excluded.

Single-class data set: This data set comprises 643 fetal brain images and has no overlap with the Multi-class data set. Shadow regions in this data set have been coarsely segmented by two bio-engineering students using trapezoid-shaped segmentation masks for individual shadow regions.

Training Data: 3448 shadow images and 3842 clear images have been randomly selected from the Multi-class data set to train the shadow/shadow-free classification network. 500 fetal brain images have been randomly chosen from the Single-class data set to train the shadow segmentation network, and the confidence estimation network. These 500 fetal images have been flipped as data augmentation during training.

Validation and Test Data: The remaining 491 shadow images and 502 clear images in the Multi-class data set are used for testing and validation. Here, a subset (M_{test}) from the 491 shadow images, comprising 48 randomly selected non-brain images, are used for testing. Shadow regions in these 48 images have been manually segmented to provide ground truth. The remaining 443 shadow images and 502 clear images are used for the validation of the shadow/shadow-free classification. Similarly, the remaining 143 fetal brain images of the Single-class data set are split into two subsets, where S_{val} contains 50 images for validation of the shadow segmentation, binary-to-confidence transformation and the confidence estimation, and S_{test} with 93 images for testing. For all images from the Single-class data set, we randomly choose one annotation from two different existing annotations as ground truth for training and testing.

B. Baseline

The baseline comprises a shadow segmentation network and a confidence estimation network, which have the same architectures as in the proposed method. We firstly train the shadow segmentation network in the baseline using the 500 fetal brain images from the Single-class data set. After applying the transfer function on the binary segmentation prediction, we train the confidence estimation network for a direct mapping between shadow images and reference confidence maps. The baseline is used to demonstrate that the multi-task module is of importance for capturing generalized shadow features and obtaining accurate confidence estimation of shadow regions.

TABLE I: Shadow segmentation performance ($\mu \pm \sigma$) of different methods on test data S_{test} . RW, RW* and Pilot are the state-of-the-art. Baseline, Proposed and Proposed+AG are the proposed methods. Anno* refers to the human inter-observer variability, thus expected human performance.

Methods		DICE	Recall	Precision	MSE
RW [15]	$\bar{\mu}$ (σ)	0.2096 (0.099)	0.6535 (0.2047)	0.1288 (0.0675)	194.8618 (7.6734)
RW* [15]	$\bar{\mu}$ (σ)	0.231 (0.1123)	0.6921 (0.2196)	0.1432 (0.0771)	189.0828 (8.3484)
Pilot [21]	$\bar{\mu}$ (σ)	0.3227 (0.1398)	0.4275 (0.201)	0.2863 (0.1352)	110.2959 (14.837)
Baseline	$\bar{\mu}$ (σ)	0.6933 (0.212)	0.6884 (0.2255)	0.7246 (0.2326)	60.3680 (12.2885)
Proposed	$\bar{\mu}$ (σ)	0.7167 (0.1988)	0.7217 (0.2131)	0.7382 (0.2255)	58.6974 (11.867)
Proposed+AG	$\bar{\mu}$ (σ)	0.7027 (0.2014)	0.7199 (0.2169)	0.7132 (0.2247)	61.241 (12.6317)
Anno*	$\bar{\mu}$ (σ)	0.5443 (0.2635)	0.6126 (0.3196)	0.567 (0.3124)	65.7286 (23.0339)

C. Evaluation Metrics

In this section, we define the aforementioned statistical metrics and compute the inter-observer variability between two pixel-wise manual annotations of shadow regions.

DICE, Recall, Precision and MSE: We refer to the binary prediction of shadow segmentation as P and the binary manual segmentation as G . $DICE = 2|P \cap G|/(|P| + |G|)$, $Recall = |P \cap G|/|G|$, $Precision = |P \cap G|/|P|$ and $MSE = |P - G|$.

ICC: We use *ICC* as proposed by [30] (Eq. 3) to measure the agreement between two annotations. Each pixel in an image is regarded as a target. R_{MS} , C_{MS} and M_{MS} are respectively mean squared value of rows, columns and interaction. N is the number of targets.

$$ICC = \frac{R_{MS} - M_{MS}}{R_{MS} + M_{MS} + 2 \times (C_{MS} - M_{MS})/N}. \quad (3)$$

Soft DICE: Since soft DICE can be used to tackle probability maps, we use float values in the DICE definition to compute soft DICE between the predicted shadow confidence maps \hat{Y}^C and reference confidence maps Y^C .

Human Performance: We consider another manual segmentation of shadow regions from a different annotator as Y_{new}^S . The computed metrics between Y_{new}^S and the chosen manual segmentation Y^S reflects the human inter-observer variability.

D. Shadow Segmentation Analysis

We compare the segmentation performance of the state-of-the-art ([15] and [21]), the proposed methods and the human performance. This comparison is used to examine the importance of the multi-task module for the shadow segmentation, and further, for the confidence estimation of shadow regions.

Table I shows DICE, recall, precision and MSE of different methods on S_{test} . RW and RW* are results of [15] with various parameters. For fair comparison, we run 24 tests on both test sets using the RW algorithm with different

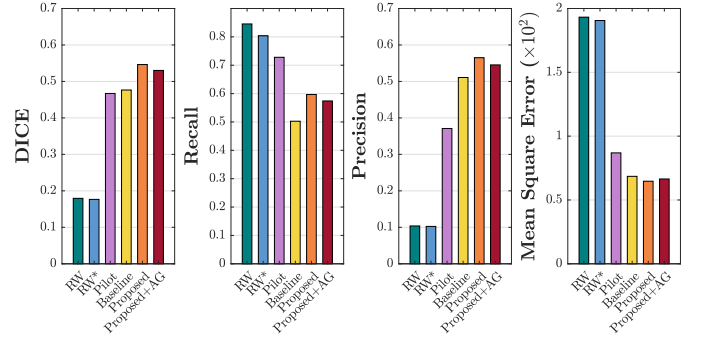


Fig. 4: Comparison of segmentation performance of different methods on test data M_{test} . The bar charts show the mean value of DICE, recall, precision and MSE of the state-of-the-art methods as well as the proposed methods.

parameter combinations ($\alpha \in \{1, 2, 6\}$; $\beta \in \{90, 120\}$; $\gamma \in \{0.05, 0.1, 0.2, 0.3\}$), and chose the parameters which achieve the highest average DICE on all samples in both test sets. The chosen RW parameters are $\alpha = 1$; $\beta = 90$; $\gamma = 0.3$. We also applied the parameters in [15] ($\alpha = 2$; $\beta = 90$; $\gamma = 0.05$) to our experiments, which is denoted as RW*. Pilot refers to our previous work in [21] and Anno* represents the human performance on the shadow segmentation task.

As shown in Table I, the baseline, the proposed method and the proposed method with attention gates (abbreviated as “the proposed+AG” in the rest of the paper) greatly outperform the state-of-the-art. Among all methods, the proposed method achieves highest DICE. Recall and precision of the proposed method are respectively 3.33% and 1.16% higher than that of the baseline. For the MSE, the proposed method is 1.67 lower than that of the baseline. After adding attention gates to the proposed method (the proposed+AG), the shadow segmentation performance is nearly the same to the proposed method without attention gates, but better than the baseline. Additionally, the relatively low scores of Anno* indicate high inter-observer variability and how ambiguous human annotation can be for this task. A mean DICE of 0.7167 shows that the proposed method performs better and more consistent than human annotation.

We further conduct the same experiments on another non-brain test data set M_{test} to verify the feature generalization ability of the multi-task module. M_{test} contains various fetal anatomies (except fetal brain), such as abdomen, kidney, cardiac and etc. Results of the same evaluation metrics are shown in Fig. 4. Similarly, the proposed weakly supervised methods and the baseline outperform all state-of-the-art methods.

E. Shadow Confidence Estimation

In this part, we evaluate the performance of the confidence estimation by comparing the shadow confidence maps of different methods.

Fig. 7 compares the shadow confidence maps of the state-of-the-art methods and the proposed methods. RW and RW* have the same parameters as used for Table I. The shadow confidence maps of the baseline, the proposed method and

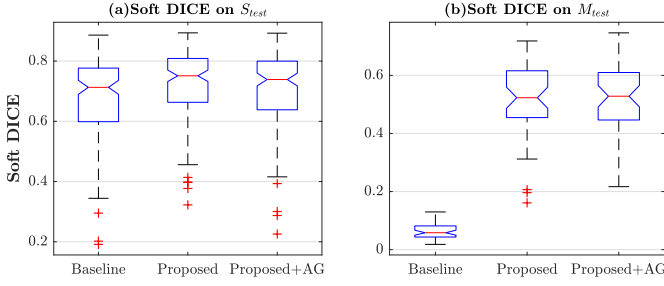


Fig. 5: Soft DICE of the baseline, the proposed method and the proposed method with attention gates (proposed+AG) on S_{test} and M_{test} .

the proposed+AG method are generated directly from input shadow images by confidence estimation networks. Overall, the proposed method and the proposed+AG method achieve better shadow confidence estimation than the baseline and the state-of-the-art on different anatomical structures shown in Fig. 7. The proposed method and the proposed+AG method are able to highlight multiple shadow regions while the RW algorithm shows limitations for most cases especially for disjoint shadow regions.

Row I in Fig. 7 is a fetal brain image from S_{test} . The confidence estimation of shadow regions from the baseline, the proposed method and the proposed+AG method are similarly accurate since we use fetal brain images to train the confidence estimation networks in these three methods. These outperform [15] and [21]. Row (II-IV) in Fig. 7 are shadow confidence maps of non-brain anatomy from M_{test} , including lips, abdomen and cardiac. The baseline failed on unseen data during inference. However, the proposed methods are able to generate accurate shadow confidence maps because of the generalized shadow features obtained by the multi-task module. Furthermore, the “Lip” example shows that our method is capable of detecting weaker shadow regions that have not been annotated in manual segmentation. This indicates that the confidence estimation network have learned general properties of shadow regions.

Fig. 5 (a) shows the soft DICE evaluation on S_{test} while (b) shows that on M_{test} . The proposed method and the proposed+AG method achieve higher soft DICE on both test

sets than the baseline, and are more robust than the baseline on M_{test} . The baseline fails in this experiment on M_{test} because the baseline is unable to obtain accurate shadow segmentation in the previous step (shown in Fig. 4). With less accurate shadow segmentation, the shadow confidence estimation can hardly establish a valid mapping between input images and reference confidence maps. This demonstrates that the multi-task module is beneficial to shadow segmentation and confidence estimation of shadow regions.

We additionally evaluate the reliability of the shadow confidence estimation by measuring the agreement between the decision of each method and the manual segmentation. Regarding the baseline, the proposed and the proposed+AG as different judges and the manual segmentation of shadow regions as a contrasting judge, we use the ICC to measure the agreement between each different judge and the contrasting judge. Fig. 6 shows the ICC evaluation on two test data sets, which indicate that the proposed method and the proposed+AG are more consistent on estimating shadow confidence maps compared with the baseline. When considering another manual segmentation of shadow regions as an extra judge, we can evaluate the agreement of human annotations. The Anno in Fig. 6 shows that the ICC of two human annotations is normally 0.51. The proposed method with an ICC of 0.66 is more consistent than annotations from two human annotators.

F. Runtime

For the RW algorithm [15] and the previous work [21], the inference time are 0.4758s and 11.35s respectively. Since the baseline, the proposed method and the proposed+AG method have the same confidence estimation networks, they have the same inference time, which is 0.0353s. These inference times show that our method is about 10 times faster than [15] and much faster than [21], which indicates that our proposed method is able to offer low-overhead real-time feedback in clinical practice.

V. APPLICATIONS

To verify the practical benefits of our method, we integrate the shadow confidence maps into different applications such as 2D US standard plane classification, multi-view image fusion and automated biometric measurements.

A. Ultrasound Standard Plane Classification

Classifying 2D fetal standard planes is of great importance for early detection of abnormalities during mid-pregnancy [28]. However, distinguishing different standard planes is a challenging task and requires intense operator training and experience. Baumgartner et al. [3] have proposed a deep learning method for the detection of various fetal standard planes. In our application, we extend [3] and utilize the confidence estimation of shadow regions to provide extra information for standard plane classification.

The data is the same as used in [3], which is a set of 2694 2D ultrasound examinations between 18-22 weeks of

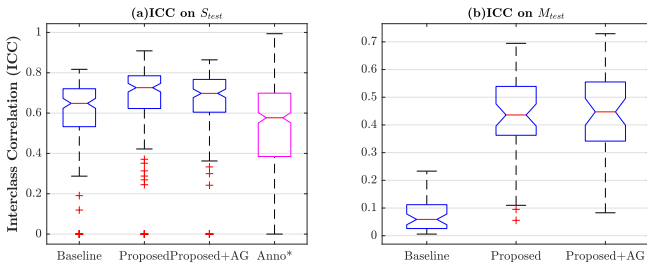


Fig. 6: Interclass correlation (ICC) of the baseline, the proposed method and the proposed method with attention gates (proposed+AG) on S_{test} and M_{test} . Additionally, ICC of the human performance is shown as Anno* for S_{test} .

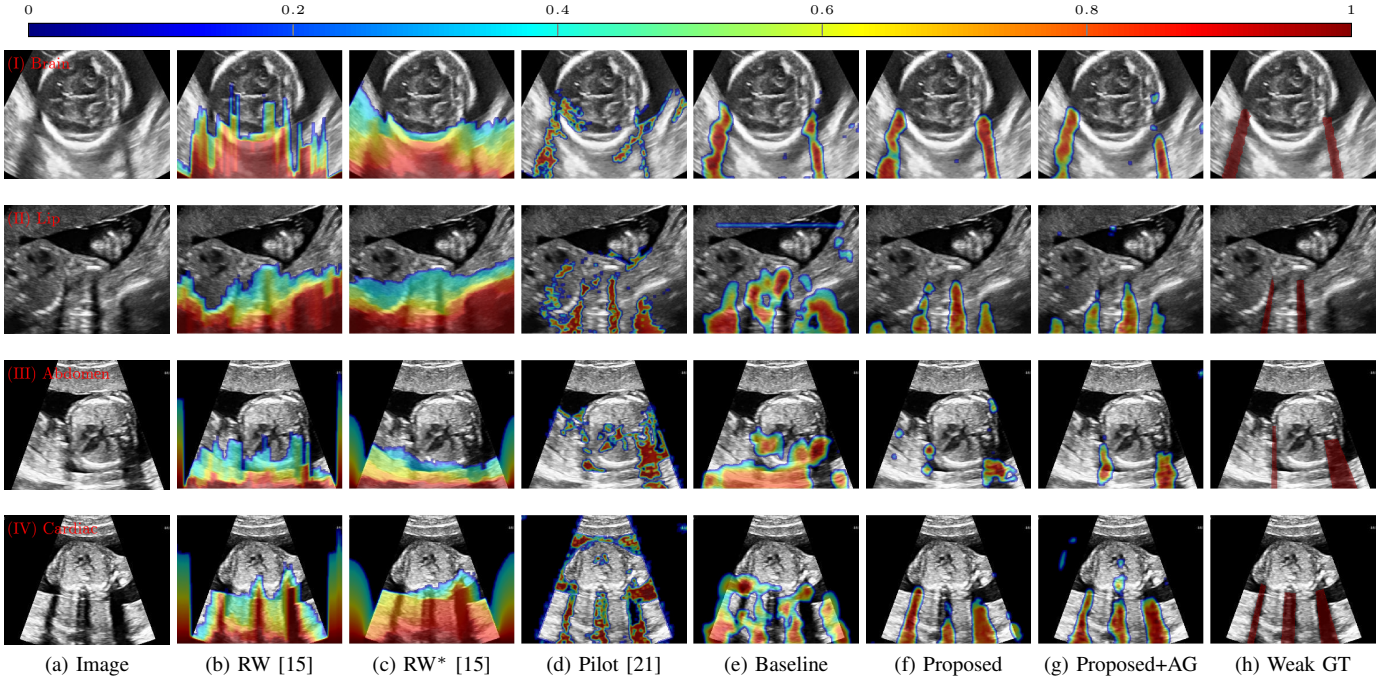


Fig. 7: Confidence estimation of shadow regions using the state-of-the-art methods and the proposed methods. Rows I-IV show four examples: Brain (top), Lip (middle), Abdomen (third) and Cardiac (bottom). Columns (b-d) are shadow confidence maps from RW algorithm [15] and our previous work [21]. Columns (e-f) are the proposed method and the proposed method with attention gate (Proposed+AG). (g) is the binary map of manual segmentation.

gestation. We select nine categories of standard planes including Three Vessel View (3VV), Four Chamber View (4CH), Abdominal, Brain View at the level of the cerebellum (Brain (cb.)), Brain view at posterior horn of the ventricle (Brain (tv.)), Femur, Lips, Left Ventricular Outflow Tract (LVOT) and Right Ventricular Outflow Tract (RVOT). The data set is split into training (16089), validation (450), and testing (4368) images, similar to [3] (see appendix E for individual class split numbers). We use image whitening (subtracting the mean intensity and divide by the variance) on each image to preprocess the whole data set.

Four networks based on SonoNet-32 [3] are built, trained and tested in order to verify the utility of shadow confidence maps. The first network is trained with the standard plane images from the training data. The next three networks are separately trained with standard plane images and their corresponding shadow confidence maps obtained by the baseline, the proposed method and the proposed+AG method. Thus, the training data in the first network has one channel while the remaining networks have two input channels. We train these networks for 75 epochs with a learning rate of 0.001.

Table II shows the standard plane classification performance of the four networks. Here, *w/o CM* is the network without shadow confidence maps while CM_B , CM_P , CM_{PAG} are networks with shadow confidence maps from the baseline, the proposed method and the proposed+AG method. Networks with shadow confidence maps achieve higher classification accuracy on almost all categories (except Abdominal, LVOT and RVOT, which are at peak performance), as well as on average classification accuracy. When the shadow confidence

TABLE II: Classification accuracy (%) with vs. without shadow confidence maps.

Class	w/o CM	CM_B	CM_P	CM_{PAG}
3VV	80.87	89.93	88.93	92.62
4CH	94.50	100.00	98.38	100.00
Abdominal	100.00	99.82	99.28	99.82
Brain(Cb.)	100.00	99.84	100.00	100.00
Brain(Tv.)	99.11	99.78	99.78	99.89
Femur	99.04	99.81	99.81	99.81
Lips	98.29	99.81	100.00	99.81
LVOT	97.90	93.69	94.29	95.80
RVOT	95.95	93.24	92.57	94.93
Avg.	97.37	98.24	98.03	98.74

maps are obtained by the proposed+AG method, the classification accuracy is highest for five categories (3VV, 4CH, Brain(Cb.), Brain(Tv.) and Femur). These results indicate that shadow confidence maps are able to provide extra information for other automatic medical image analysis algorithms and to improve their performance.

B. Multi-view Image Fusion

Routine US screening is usually performed using a single 2D probe. However, the position of the probe and resulting tomographic view through the anatomy has great effects on diagnosis. [34] proposed a multi-view image reconstruction method, which compounds different images of the same anatomical structure acquired from different view directions. [34] uses a Gaussian weighting strategy to blend intensity information from difference views. Here, we combine predicted

TABLE III: Biometric measurement performance (DICE) with VS. without shadow confidence maps.

	w/o CM	CM _B	CM _P	CM _{PAG}
#1	0.947	0.940	0.988	0.969
#2	0.956	0.958	0.974	0.968
#3	0.880	0.915	0.923	0.955
Avg.	0.966	0.964	0.965	0.964

shadow confidence maps from these multi-view images as additional image fusion weights to find if these confidence maps can further improve image quality. Fig. 8 qualitatively shows that shadow confidence maps are able to improve the performance of image fusion with different weighting strategies. Fig. 8 also shows the difference between adding two different types of confidence maps. These two types of confidence maps are generated by the confidence estimation network which are separately trained by MSE and Sigmoid loss. Quantitative evaluation for image fusion is not possible because of lacking ground truth for US compounding tasks.

C. Automated Biometric Measurements

We integrate our shadow confidence maps into an automatic biometric measurement approach [31], and show biometric measurement performance (measured by DICE) before and after adding shadow confidence maps. We show three examples that are affected by shadows, and show their biometric measurement results in Table III. From this experiment, we find that biometric measurement performance is boosted by up to 7% for problematic failure cases after adding shadow confidence maps. The average performance on the entire test data set stays almost the same since only a small proportion of the test images are affected by strong shadows, mainly because of image acquisition by highly skilled sonographers.

VI. DISCUSSION

In this paper, we propose a weakly supervised method to tackle the ill-defined problem of shadow detection in US. A naïve alternative to our method would be to train a fully supervised shadow segmentation network using pixel-wise annotation of shadow regions. However, pixel-wise annotation is infeasible because (a) accurately annotating a large number of images requires a vast amount of labour and time and introduces scanner dependencies (b) binary annotations of shadow regions would lead to high inter-observer variability as shadow features are poorly defined, and (c) continuous annotations of shadow regions are affected by subjectivity of annotators.

The performance of shadow region confidence estimation on different anatomical structures can be improved after integrating attention mechanisms. For example, the soft DICE is increased on S_{test} . This also results in improved ultrasound classification (Table. II). However, the quantitative results of shadow segmentation on both test data sets show that attention mechanisms are not essential. Networks with attention mechanisms are sometimes outperformed by networks without attention mechanisms. This may be caused by the way we

integrate the attention mechanism. Since we add attention gates to encoders of all networks, the shadow features are emphasized for the shadow/shadow-free classification, which increases the difficulty of generalizing shadow features from classification to shadow segmentation.

We use MSE as the loss function of the confidence estimation network, but this loss can also be measured by other functions. Practically this choice has no effect on our quantitative results. However, in the image fusion task, we observe qualitative differences, which we show in Fig. 8 for Sigmoid cross entropy loss.

In the standard plane classification task, we use only a subset of target standard planes compared to [3] because (1) we aim at verifying the usefulness of our method rather than improving performance of [3], (2) it is desirable to keep inter-class balance to avoid side-effects from under-represented classes, and (3) we chose standard planes for which [3] did not show optimal classification performance.

$T(\cdot)$, as defined in Sec. II is one example how prior knowledge can be integrated into the training process of confidence map estimation. If $T(\cdot)$ is chosen to be a continuous non-trainable function, e.g. quadratic or Gaussian, further weight relaxation can be introduced for joint refinement of both, the multi-task module in Fig. 1a and the confidence estimation in Fig. 1c. However, since probabilistic ground truth does not exist for our applications, evaluation would become purely subjective, thus we decide to use direct but discontinuous integration of shadow-intensity assumptions for $T(\cdot)$.

Task-specific deep networks may inadvertently learn to ignore weak shadows in some cases, but the learning capacity of shadow properties is unknown. By estimating confidence of shadow regions independently, our method guarantees that shadow property information is separately extracted and can be seamlessly integrated into other image analysis algorithms. With additional shadow property information, our method can improve steerability and interpretability for deep neural networks, and also enables extensions for non-deep learning algorithms. As shown in the experiments, prior knowledge as provided by shadow confidence maps can improve the performance of various applications.

VII. CONCLUSION

We propose a CNN-based, weakly supervised method for automatic confidence estimation of shadow regions in 2D US images. By learning and transferring shadow features from weakly-labelled images, our method can predict dense, continuous shadow confidence maps directly from input images.

We evaluate the performance of our method by comparing it to the state-of-the-art and human performance. Our experiments show that, for confidence estimation of shadow regions, our method is qualitatively and quantitatively better than the state-of-the-art and is more consistent than human annotation. More importantly, our method is capable of detecting disjoint multiple shadow regions without being limited by (1) the correlation between adjacent pixels as in [15], and (2) the heuristically selected hyperparameters in [21].

We further demonstrate that our method improves the performance of other automatic image analysis algorithms when

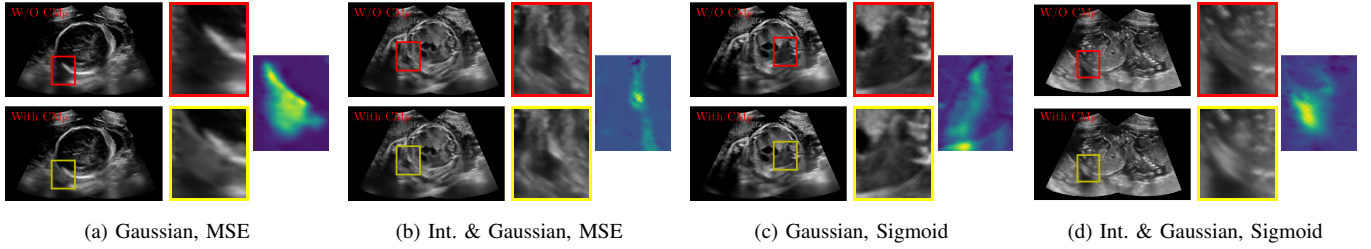


Fig. 8: Results of image fusion with Gaussian weighting (a,c) vs. Intensity and Gaussian weighting (b,d) and MSE loss (a-b) vs. Sigmoid loss (c-d). Top row is without integrating a shadow confidence map CM_P and bottom row is with integrated CM_P . Framed areas show enlarged sections of the images. Middle row are the difference maps of corresponding framed areas.

integrating the obtained shadow confidence maps into other US applications such as standard plane classification, image fusion and automated biometric measurements.

Our method has significantly shorter inference time compared with the state-of-the-art, which enables real-time feedback of local image properties. This real-time feedback can guide inexperienced sonographers to find diagnostically valuable viewing directions and pave the way for standardized image acquisition training.

REFERENCES

- [1] J. Abbott and F. Thurstone. Acoustic speckle: Theory and experimental analysis. *Ultrasonic Imaging*, 1(4):303–324, 1979.
- [2] P. Anbeek, K. L. Vincken, G. S. van Bochove, M. J. van Osch, and J. van der Grond. Probabilistic segmentation of brain tissue in mr imaging. *NeuroImage*, 27(4):795 – 804, 2005.
- [3] C. Baumgartner, K. Kamnitsas, J. Matthew, T. P. Fletcher, S. Smith, L. M. Koch, B. Kainz, and D. Rueckert. Sononet: Real-time detection and localisation of fetal standard scan planes in freehand ultrasound. *IEEE Trans. Med. Imag.*, 36:2204–2215, 2017.
- [4] C. Baumgartner, L. Koch, K. Tezcan, J. Ang, and E. Konukoglu. Visual feature attribution using wasserstein gans. *CoRR*, abs/1711.08998, 2017.
- [5] F. Berton, F. Cheriet, M. M., and C. Laporte. Segmentation of the spinous process and its acoustic shadow in vertebral ultrasound images. *Computers in Biology and Medicine*, 72:201–211, 2016.
- [6] B. Bouhemad, M. Zhang, Q. Lu, and J. Rouby. Clinical review: bedside lung ultrasound in critical care practice. *Critical Care*, 11(1):205, 2007.
- [7] A. Broersen, M. Graaf, J. Eggermont, R. Wolterbeek, P. Kitslaar, J. Dijkstra, J. Bax, J. Reiber, and A. Scholte. Enhanced characterization of calcified areas in intravascular ultrasound virtual histology images by quantification of the acoustic shadow: validation against computed tomography coronary angiography. *Int J Cardiovasc Imaging*, 32:543–552, 2015.
- [8] Centre for Workforce Intelligence. Securing the future workforce supply sonography workforce review. 2017.
- [9] H. Choi, J. Lee, S. Kim, and S. Park. Speckle noise reduction in ultrasound images using a discrete wavelet transform-based image fusion technique. *Bio-Medical Materials and Engineering*, 26(1):1587–1597, 2015.
- [10] P. Coupé, P. Hellier, C. Kervrann, and C. Barillot. Non-local means-based speckle filtering for ultrasound images. *IEEE Trans. Image Process.*, 18(10):2221–2229, 2009.
- [11] L. R. Dice. Measures of the amount of ecologic association between species. *Ecology*, 26(3):297–302, 1945.
- [12] M. K. Feldman, S. Katyal, and M. S. Blackwood. Us artifacts. *Radio Graphics*, 29:11791189, 2009.
- [13] K. He, X. Zhang, S. Ren, and J. Sun. Identity mappings in deep residual networks. In *ECCV*, pages 630–645. Springer, 2016.
- [14] P. Hellier, P. Coupé, X. Morandi, and D. Collins. An automatic geometrical and statistical method to detect acoustic shadows in intraoperative ultrasound brain images. *Med Image Anal*, 14(2):195–204, 2010.
- [15] A. Karamalis, W. Wein, T. Klein, and N. Navab. Ultrasound confidence maps using random walks. *Med Image Anal*, 16(6):1101–1112, 2012.
- [16] H. Kim and T. Varghese. Hybrid spectral domain method for attenuation slope estimation. *Ultrasound Med Biol*, 34:1808–1819, 2008.
- [17] T. Klein and W. Wells. Rf ultrasound distribution-based confidence maps. In *MICCAI’15*, pages 595–602. Springer, 2015.
- [18] F. W. Kremkau and K. Taylor. Artifacts in ultrasound imaging. *J Ultrasound Med*, 5(4):227–237, 1986.
- [19] A. Krizhevsky, I. Sutskever, and G. Hinton. Imagenet classification with deep convolutional neural networks. In *NIPS’12*, pages 1097–1105, 2012.
- [20] T. Lange, N. Papenberg, S. Heldmann, J. Modersitzki, B. Fischer, H. Lamecker, and P. Schlag. 3D ultrasound-CT registration of the liver using combined landmark-intensity information. *Int J Comput Assist Radiol Surg*, 4(1):79–88, 2009.
- [21] Q. Meng, C. Baumgartner, M. Sinclair, J. Housden, M. Rajchl, A. Gomez, B. Hou, N. Toussaint, V. Zimmer, J. Tan, et al. Automatic shadow detection in 2d ultrasound images. In *MICCAI Workshop on PIPPI*, 2018.
- [22] NHS. *Fetal anomaly screening programme: programme handbook June 2015*. Public Health England, 2015.
- [23] J. A. Noble. Ultrasound image segmentation and tissue characterization. *Proc Inst Mech Eng H.*, 224(2):307–316, 2010.

- [24] O. Oktay, J. Schlemper, L. L. Folgoc, M. Lee, M. P. Heinrich, K. Misawa, K. Mori, S. G. McDonagh, N. Y. Hammerla, B. Kainz, et al. Attention u-net: Learning where to look for the pancreas. *CoRR*, abs/1804.03999, 2018.
- [25] N. Pawlowski, S. I. Ktena, M. Lee, B. Kainz, D. Rueckert, B. Glocker, and M. Rajchl. Dltk: State of the art reference implementations for deep learning on medical images. *arXiv preprint arXiv:1711.06853*, 2017.
- [26] G. P. Penney, J. M. Blackall, M. S. Hamady, T. Sabharwal, A. Adam, and D. J. Hawkes. Registration of freehand 3d ultrasound and magnetic resonance liver images. *Med Image Anal*, 8:81–91, 2004.
- [27] M. Rajchl, M. Lee, O. Oktay, K. Kamnitsas, J. Passerat-Palmbach, W. Bai, M. Damodaram, M. Rutherford, J. Hajnal, B. Kainz, et al. Deepcut: Object segmentation from bounding box annotations using convolutional neural networks. *IEEE Trans. Med. Imag.*, 36(2):674–683, 2017.
- [28] L. J. Salomon, Z. Alfrevic, V. Berghella, C. Bilardo, E. Hernandez-Andrade, S. L. Johnsen, K. Kalache, K. Leung, G. Malinger, H. Munoz, et al. Practice guidelines for performance of the routine midtrimester fetal ultrasound scan. *Ultrasound Obst Gyn*, 37:116–126, 2011.
- [29] T. Shen, T. Zhou, G. Long, J. Jiang, S. Pan, and C. Zhang. Disan: Directional self-attention network for rnn/cnn-free language understanding. In *AAAI*, 2018.
- [30] P. E. Shrout and J. L. Fleiss. Intraclass correlations: Uses in assessing rater reliability. *Psychol Bull.*, 86(2):420–428, 1979.
- [31] M. Sinclair, C. Baumgartner, J. Matthew, W. Bai, J. Cerrolaza, Y. Li, S. Smith, C. Knight, B. Kainz, J. Hajnal, et al. Human-level performance on automatic head biometrics in fetal ultrasound using fully convolutional neural networks. In *EMBC’18*, 2018.
- [32] J. Springenberg, A. Dosovitskiy, T. Brox, and M. Riedmiller. Striving for simplicity: The all convolutional net. *CoRR*, abs/1412.6806, 2014.
- [33] R. Steel, T. L. Poepping, R. S. Thompson, and C. Macaskill. Origins of the edge shadowing artefact in medical ultrasound imaging. *Ultrasound Med Biol*, 39:1153–1162, 2005.
- [34] A. Z. Veronika, G. Alberto, N. Yohan, T. Nicolas, K. Bishesh, W. Robert, P. Laura, V. P. Milou, S. Emily, M. Jacqueline, et al. Multi-view image reconstruction: Application to fetal ultrasound compounding. In *MICCAI Workshop on PIPPI*, 2018.
- [35] A. C. Wilson, R. Roelofs, M. Stern, N. Srebro, and B. Recht. The marginal value of adaptive gradient methods in machine learning. *CoRR*, abs/1705.08292, 2018.
- [36] B. Zhou, A. Khosla, A. Lapedriza, A. Oliva, and A. Torralba. Learning deep features for discriminative localization. In *CVPR’16*, pages 2921–2929. IEEE, 2016.

APPENDIX

A. Shadow/Shadow-free Classification Network

In this section, we use Python-inspired pseudo code to present the detailed network architecture of the shadow/shadow-free classification network (shown in Fig. 9). The `conv_layer` function performs a standard 2D convolution without activation layer and the `global_average_pool` operates spatial averaging on the feature maps. The `residual_block` is realized by DLTK [25].

```
def classification_network(image):
    # inputs:
    # image: images has shadow (l=1) or images without shadow (l=0)

    # output:
    # logits: the output of the classification network

    feature_1 = conv_layer(image, num_filters=16, kernel_size=(3,3), strides=(1,1))
    feature_2_1 = residual_block(feature_1, num_filters=32, kernel_size=(3,3), strides=(2,2))
    feature_2_2 = residual_block(feature_2_1, num_filters=32, kernel_size=(3,3), strides=(1,1))
    feature_3_1 = residual_block(feature_2_2, num_filters=64, kernel_size=(3,3), strides=(2,2))
    feature_3_2 = residual_block(feature_3_1, num_filters=64, kernel_size=(3,3), strides=(1,1))
    feature_4_1 = residual_block(feature_3_2, num_filters=128, kernel_size=(3,3), strides=(2,2))
    feature_4_2 = residual_block(feature_4_1, num_filters=128, kernel_size=(3,3), strides=(1,1))
    feature_5 = conv_layer(feature_4_2, num_filters=2, kernel_size=(1,1), strides=(1,1))
    logits = global_average_pool(feature_5, axis=(1,2))

    return logits
```

Fig. 9: Shadow/shadow-free classification network architecture.

B. Shadow Segmentation Network

Fig.10 shows the detailed architecture of the segmentation network. The `conv_layer` function performs a standard 2D convolution without activation layer. The `residual_block` and the `upsample_concat` (the upsampling and concatenation layer) are realized by DLTK [25].

```
def segmentation_network(image):
    # inputs:
    # image: images has shadow (l=1) and additive weak pixel-wise manual segmentation

    # output:
    # logits: the output of the shadow segmentation network

    # encoder
    feature_1 = conv_layer(image, num_filters=8, kernel_size=(3,3), strides=(1,1))
    feature_2_1 = residual_block(feature_1, num_filters=16, kernel_size=(3,3), strides=(2,2))
    feature_2_2 = residual_block(feature_2_1, num_filters=16, kernel_size=(3,3), strides=(1,1))
    feature_3_1 = residual_block(feature_2_2, num_filters=32, kernel_size=(3,3), strides=(2,2))
    feature_3_2 = residual_block(feature_3_1, num_filters=32, kernel_size=(3,3), strides=(1,1))
    feature_4_1 = residual_block(feature_3_2, num_filters=64, kernel_size=(3,3), strides=(2,2))
    feature_4_2 = residual_block(feature_4_1, num_filters=64, kernel_size=(3,3), strides=(1,1))

    # decoder
    feature_5_1 = upsample_concat(feature_4_2, num_filters=32, strides=(2,2))
    feature_5_2 = residual_block(feature_5_1, num_filters=32, kernel_size=(3,3), strides=(1,1))
    feature_5_3 = residual_block(feature_5_2, num_filters=32, kernel_size=(3,3), strides=(1,1))
    feature_6_1 = upsample_concat(feature_5_3, num_filters=64, strides=(2,2))
    feature_6_2 = residual_block(feature_6_1, num_filters=64, kernel_size=(3,3), strides=(1,1))
    feature_6_3 = residual_block(feature_6_2, num_filters=64, kernel_size=(3,3), strides=(1,1))
    feature_7_1 = upsample_concat(feature_6_3, num_filters=128, strides=(2,2))
    feature_7_2 = residual_block(feature_7_1, num_filters=128, kernel_size=(3,3), strides=(1,1))
    feature_7_3 = residual_block(feature_7_2, num_filters=128, kernel_size=(3,3), strides=(1,1))
    logits = conv_layer(feature_7_3, num_filters=2, kernel_size=(1,1), strides=(1,1))

    return logits
```

Fig. 10: Shadow segmentation network architecture.

C. Confidence Estimation Network

Fig. 11 shows the detailed architecture of the shadow confidence estimation network. Similarly, the `conv_layer`

function performs a standard 2D convolution without activation layer. The `residual_block` and the `upsample_concat` (the upsampling and concatenation layer) are realized by DLTK [25].

```
def confidence_estimation_network(image):
    # inputs:
    # image: images and additive reference confidence map
    # Note: the reference confidence map is obtained by the Transfer Matrix using
    # the output of the shadow segmentation network.

    # output:
    # logits: the output of the shadow segmentation network

    # encoder
    feature_1 = conv_layer(image, num_filters=8, kernel_size=(3,3), strides=(1,1))

    feature_2_1 = residual_block(feature_1, num_filters=16, kernel_size=(3,3), strides=(2,2))
    feature_2_2 = residual_block(feature_2_1, num_filters=16, kernel_size=(3,3), strides=(1,1))

    feature_3_1 = residual_block(feature_2_2, num_filters=32, kernel_size=(3,3), strides=(2,2))
    feature_3_2 = residual_block(feature_3_1, num_filters=32, kernel_size=(3,3), strides=(1,1))

    feature_4_1 = residual_block(feature_3_2, num_filters=64, kernel_size=(3,3), strides=(2,2))
    feature_4_2 = residual_block(feature_4_1, num_filters=64, kernel_size=(3,3), strides=(1,1))

    # decoder
    feature_5_1 = upsample_concat(feature_4_2, num_filters=32, strides=(2,2))
    feature_5_2 = residual_block(feature_5_1, num_filters=32, kernel_size=(3,3), strides=(1,1))
    feature_5_3 = residual_block(feature_5_2, num_filters=32, kernel_size=(3,3), strides=(1,1))

    feature_6_1 = upsample_concat(feature_5_3, num_filters=64, strides=(2,2))
    feature_6_2 = residual_block(feature_6_1, num_filters=64, kernel_size=(3,3), strides=(1,1))
    feature_6_3 = residual_block(feature_6_2, num_filters=64, kernel_size=(3,3), strides=(1,1))

    feature_7_1 = upsample_concat(feature_6_3, num_filters=128, strides=(2,2))
    feature_7_2 = residual_block(feature_7_1, num_filters=128, kernel_size=(3,3), strides=(1,1))
    feature_7_3 = residual_block(feature_7_2, num_filters=128, kernel_size=(3,3), strides=(1,1))

    logits = conv_layer(feature_7_3, num_filters=1, kernel_size=(1,1), strides=(1,1))

    return logits
```

Fig. 11: Shadow confidence estimation network architecture.

D. Alternative Examples of Shadow Confidence Estimation

We show an alternative group of examples for the confidence estimation of shadow regions (shown in Fig. 12). These examples include fetal brain from M_{test} , and cardiac, lip, kidney from S_{test} . Similar to the Fig. 7 in the main paper, Fig. 12 shows that the baseline fails to handle unseen data while the proposed method and the proposed+AG method are able to predict pixel-wise confidence of multiple shadow regions. These examples demonstrate that the multi-task module is able to generalize the shadow representation and transfer shadow representation from the shadow/shadow-free classification task to a confidence estimation task.

E. Data in Ultrasound Classification

Table IV shows the exact number of data used in the application of 2D US standard plane classification (Section V. Part A). The training data of each category is almost the same so that we can keep class balance between different classes during training.

F. Class Confusion Matrix

Fig. 15 additionally shows the class confusion matrix of 2D US standard plane classification in Section V. Part A. This class confusion matrix demonstrates that less 3VV images are mis-classified as RVOT images and less 4CH images are mis-classified as LVOT images after adding shadow confidence maps. However, as we discussed in the above Discuss Section, the shadow confidence maps can also introduce redundant information for similar anatomical structures in this classification task. For example, more LVOT images are wrongly classified as RVOT and more RVOT images are classified as 3VV images.

TABLE IV: Summary of the Data Set used in Ultrasound Standard Plane Classification Task.

Class	Training	Validation	Testing
3VV	1480	50	298
4CH	1544	50	309
Abdominal	2000	50	553
Brain(Cb.)	2000	50	634
Brain(Tv.)	2000	50	899
Femur	2000	50	520
Lips	2000	50	526
LVOT	1633	50	333
RVOT	1432	50	296
Sum	16089	450	4368

G. Examples for Image Fusion

Fig.13 includes the original multi-view images that are used for the image fusion task in Fig.8. From the column (a-b) of Fig.13, we can see that the original images contain strong shadow artifacts that can affect the anatomical analysis. The image fusion task aims to use complementary information from images with different views for reducing artifacts and increasing anatomical information. Column (e-f) enlarge the areas within the bounding boxes in column (c-d). Column (g) shows the difference masks between column (e) and (f). The difference masks clearly indicate the improved performance of image fusion after adding shadow confidence maps for Gaussian weighting strategy as well as Intensity and Gaussian weighting strategy.

H. Examples for Biometric Measurement

We visualize the biometric measurement of the three examples shown in Table III. Fig. 14 demonstrates that, for the cases affected by shadow artifacts, the segmentation performance (“EI_seg DICE”) is improved after adding shadow confidence maps as an extra channel. From the first row to the third row in Fig. 14, these three samples are respectively #1, #2 and #3 samples in Table.III.

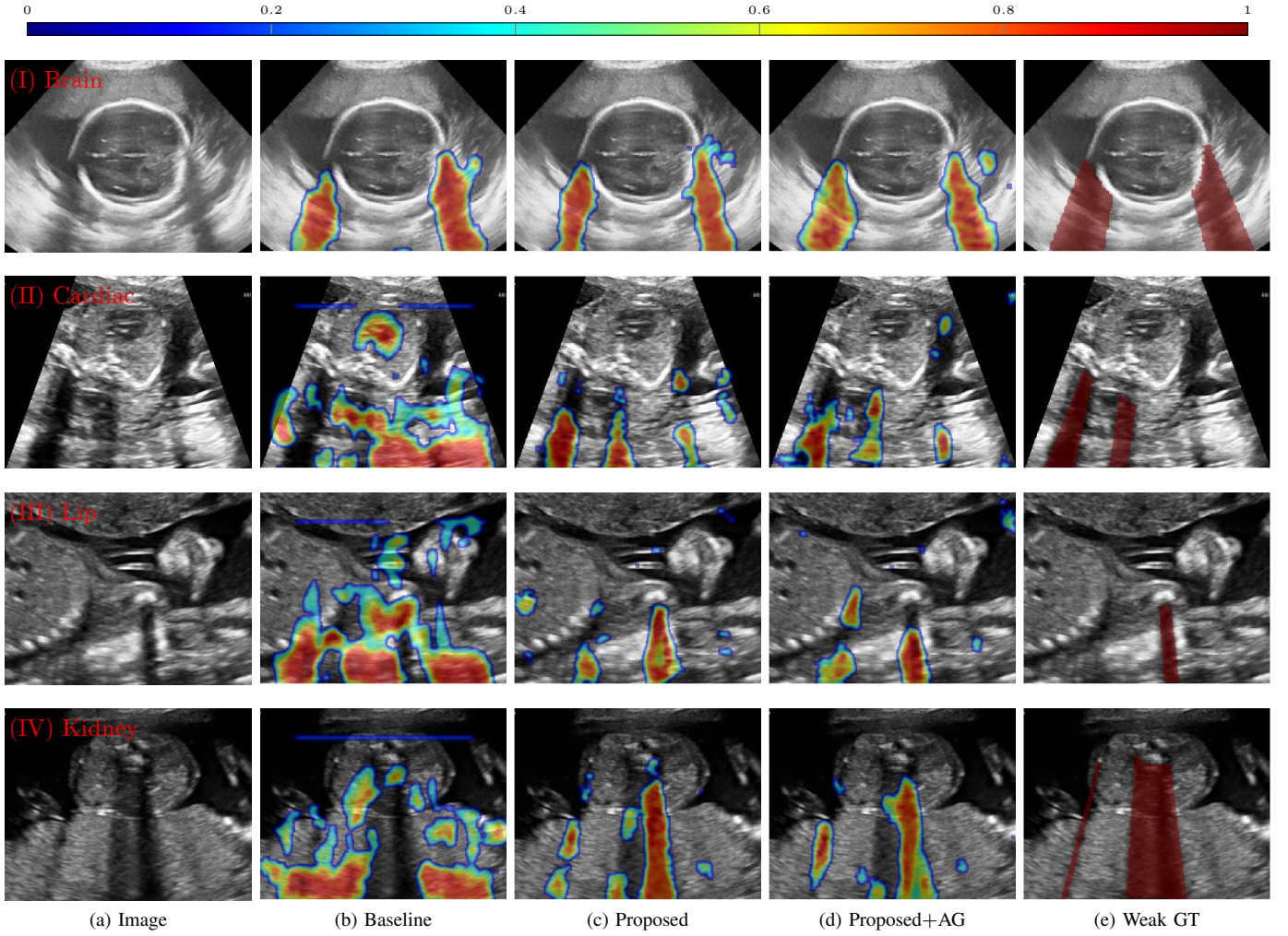


Fig. 12: Shadow confidence maps of different methods on various anatomical US images. Rows I-IV show four examples of shadow confidence estimation; Brain (top), Cardiac (middle), Lip (third) and Kidney (bottom). Columns (b-d) are shadow confidence maps from the baseline, the proposed method and the proposed method with attention gate (Proposed+AG). (f) is the binary map of manual segmentation.

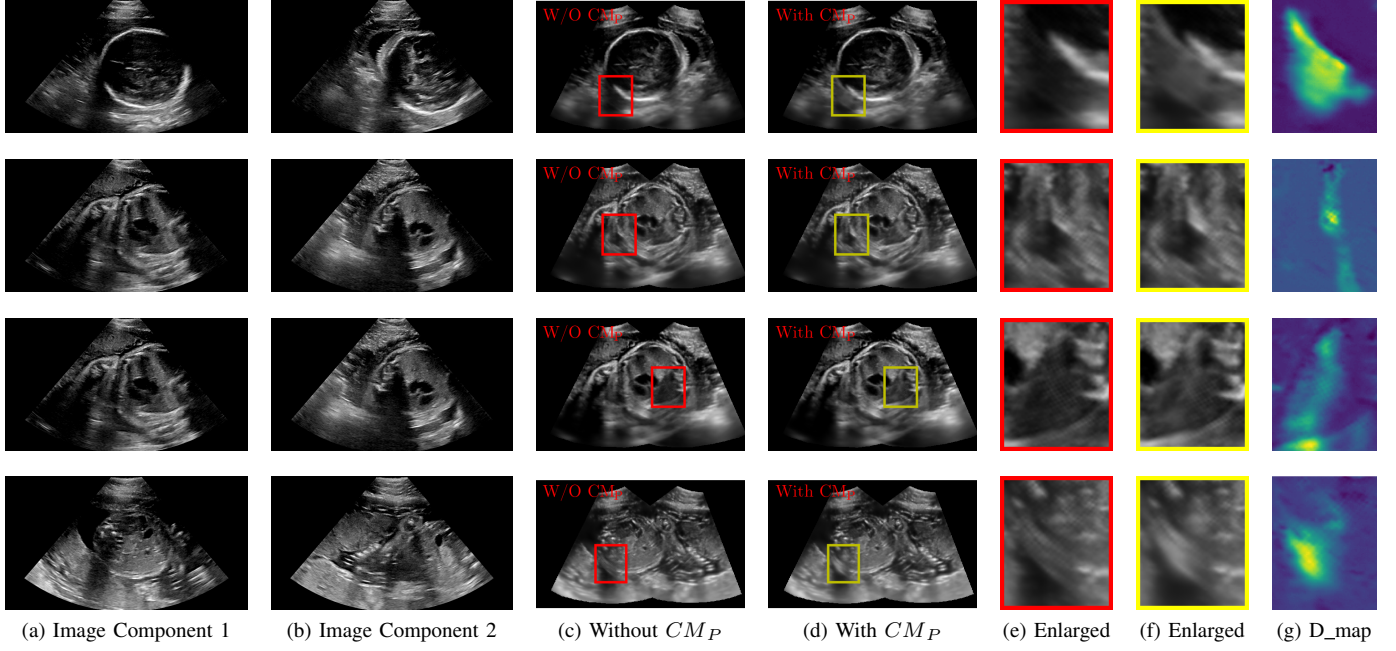


Fig. 13: The detailed results of Fig.8. (a-b) The multi-view images, (c) Image fusion without shadow confidence maps (CM_P), (d) Image fusion with shadow confidence maps (CM_P), (e-f) Enlarged areas of (c-d) respectively, and (g) Difference maps of (e) and (f). Row (1-2) use MSE loss to train networks for generating shadow confidence maps while Row (3-4) use Sigmoid loss. Row (1,3) use the Gaussian weighting for image fusion while Row (2,4) use the Intensity and Gaussian weighting.

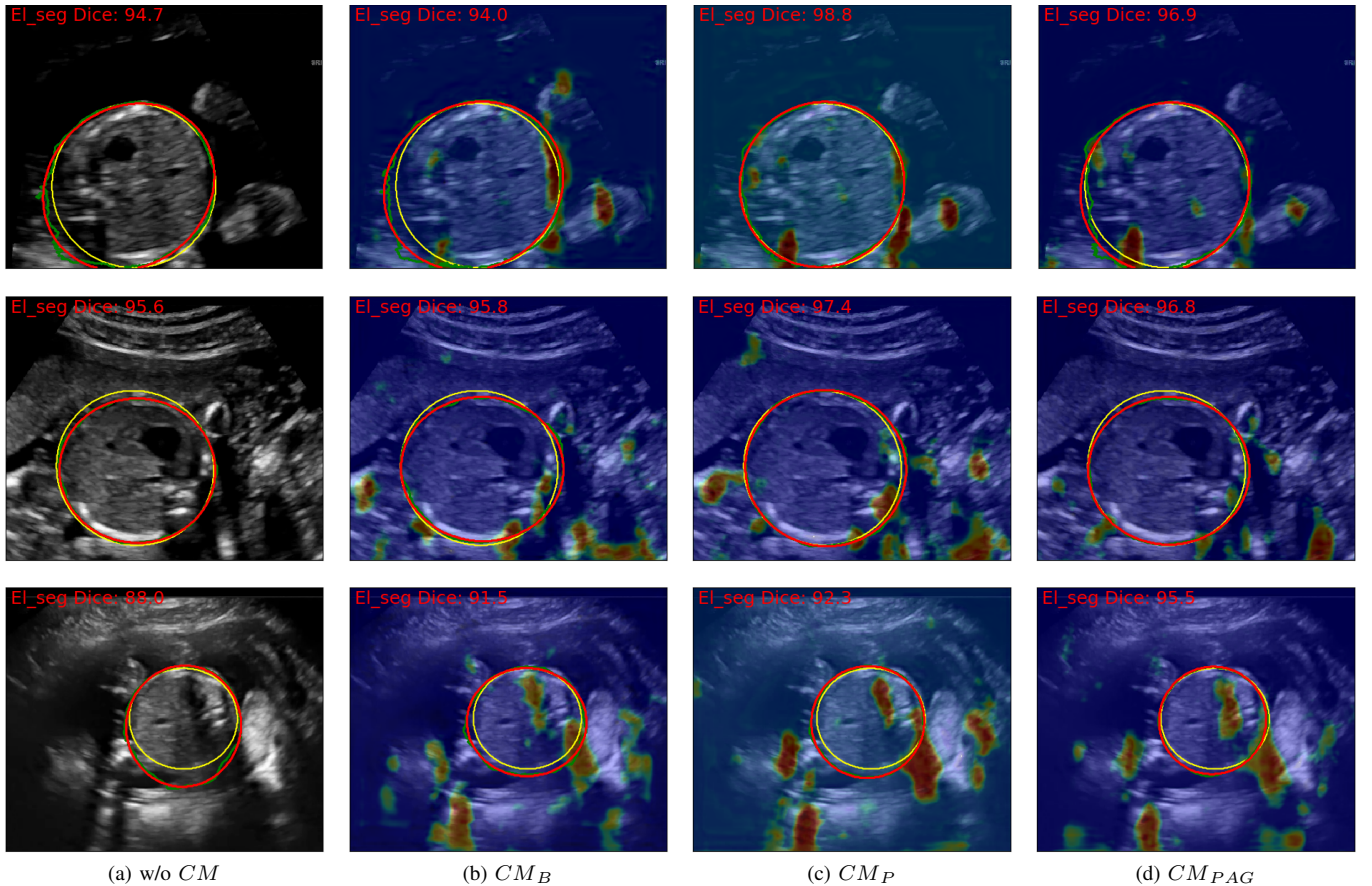


Fig. 14: Biometric measurement with VS. without shadow confidence maps. The yellow circles refer to the ground truth, the green curves are segmentation predictions, and the red circles are the ellipses of the segmentation prediction.

W/O CM (Accuracy: 97.37%)									
	Predicted label								
	3VV	4CH	Abdominal	Brain(Cb.)	Brain(Tv.)	Femur	Lips	LVOT	RVOT
3VV	80.9% 241	0.6% 2	0.0% 0	0.0% 0	0.0% 0	0.0% 0	0.3% 1	0.3% 1	
4CH	0.7% 2	94.5% 292	0.0% 0	0.0% 0	0.0% 0	0.0% 0	0.3% 1	0.0% 0	
Abdominal	0.0% 0	0.0% 0	100.0% 553	0.0% 0	0.0% 0	1.0% 5	1.3% 7	0.0% 0	0.3% 1
Brain(Cb.)	0.0% 0	0.0% 0	0.0% 0	100.0% 634	0.9% 8	0.0% 0	0.0% 0	0.3% 1	0.0% 0
Brain(Tv.)	0.0% 0	0.0% 0	0.0% 0	0.0% 0	99.1% 891	0.0% 0	0.0% 0	0.0% 0	0.0% 0
Femur	0.0% 0	0.0% 0	0.0% 0	0.0% 0	0.0% 0	99.0% 515	0.0% 0	0.0% 0	0.0% 0
Lips	0.7% 2	0.0% 0	0.0% 0	0.0% 0	0.0% 0	0.0% 0	98.3% 517	0.0% 0	0.3% 1
LVOT	1.3% 4	4.5% 14	0.0% 0	0.0% 0	0.0% 0	0.0% 0	0.4% 2	97.9% 326	3.0% 9
RVOT	16.4% 49	0.3% 1	0.0% 0	0.0% 0	0.0% 0	0.0% 0	0.0% 0	1.2% 4	95.9% 284

CM from the Baseline (Accuracy: 98.24%)									
	Predicted label								
	3VV	4CH	Abdominal	Brain(Cb.)	Brain(Tv.)	Femur	Lips	LVOT	RVOT
3VV	89.9% 268	0.0% 0	0.0% 0	0.0% 0	0.0% 0	0.0% 0	0.0% 0	0.9% 3	5.1% 15
4CH	0.0% 0	100.0% 309	0.0% 0	0.0% 0	0.0% 0	0.0% 0	0.0% 0	1.5% 5	0.3% 1
Abdominal	0.0% 0	0.0% 0	99.8% 552	0.0% 0	0.0% 0	0.2% 1	0.2% 1	0.0% 0	0.0% 0
Brain(Cb.)	0.0% 0	0.0% 0	0.0% 0	99.8% 633	0.2% 2	0.0% 0	0.0% 0	0.0% 0	0.0% 0
Brain(Tv.)	0.0% 0	0.0% 0	0.0% 0	0.2% 1	99.8% 897	0.0% 0	0.0% 0	0.0% 0	0.0% 0
Femur	0.0% 0	0.0% 0	0.2% 1	0.0% 0	0.0% 0	99.8% 519	0.0% 0	0.0% 0	0.0% 0
Lips	0.0% 0	0.0% 0	0.0% 0	0.0% 0	0.0% 0	0.0% 0	99.8% 525	0.3% 1	0.3% 1
LVOT	0.7% 2	0.0% 0	0.0% 0	0.0% 0	0.0% 0	0.0% 0	0.0% 0	93.7% 312	1.0% 3
RVOT	9.4% 28	0.0% 0	0.0% 0	0.0% 0	0.0% 0	0.0% 0	0.0% 0	3.6% 12	93.2% 276

CM from the Proposed (Accuracy: 98.03%)									
	Predicted label								
	3VV	4CH	Abdominal	Brain(Cb.)	Brain(Tv.)	Femur	Lips	LVOT	RVOT
3VV	88.9% 265	0.3% 1	0.0% 0	0.0% 0	0.0% 0	0.0% 0	0.6% 2	5.7% 17	
4CH	0.0% 0	98.4% 304	0.0% 0	0.0% 0	0.0% 0	0.0% 0	2.1% 7	0.3% 1	
Abdominal	0.0% 0	0.0% 0	99.3% 549	0.0% 0	0.0% 1	0.2% 0	0.0% 0	0.0% 0	0.0% 0
Brain(Cb.)	0.0% 0	0.0% 0	0.0% 0	100.0% 634	0.2% 2	0.0% 0	0.0% 0	0.3% 1	0.0% 0
Brain(Tv.)	0.0% 0	0.0% 0	0.0% 0	0.0% 0	99.8% 897	0.0% 0	0.0% 0	0.0% 0	0.0% 0
Femur	0.0% 0	0.0% 0	0.4% 2	0.0% 0	0.0% 0	99.8% 519	0.0% 0	0.0% 0	0.0% 0
Lips	0.0% 0	0.0% 0	0.2% 1	0.0% 0	0.0% 0	0.0% 0	100.0% 526	0.0% 0	0.3% 1
LVOT	0.7% 2	0.6% 2	0.2% 1	0.0% 0	0.0% 0	0.0% 0	0.0% 0	94.3% 314	1.0% 3
RVOT	10.4% 31	0.6% 2	0.0% 0	0.0% 0	0.0% 0	0.0% 0	0.0% 0	2.7% 9	92.6% 274

CM from the Proposed+AG (Accuracy: 98.74%)									
	Predicted label								
	3VV	4CH	Abdominal	Brain(Cb.)	Brain(Tv.)	Femur	Lips	LVOT	RVOT
3VV	92.6% 276	0.0% 0	0.0% 0	0.0% 0	0.0% 0	0.0% 0	0.0% 0	0.6% 2	4.1% 12
4CH	0.0% 0	100.0% 309	0.0% 0	0.0% 0	0.0% 0	0.0% 0	0.0% 0	1.5% 5	0.0% 0
Abdominal	0.0% 0	0.0% 0	99.8% 552	0.0% 0	0.0% 1	0.2% 0	0.0% 0	0.0% 0	0.3% 1
Brain(Cb.)	0.0% 0	0.0% 0	0.0% 0	100.0% 634	0.1% 1	0.0% 0	0.0% 0	0.3% 1	0.0% 0
Brain(Tv.)	0.0% 0	0.0% 0	0.0% 0	0.0% 0	99.9% 898	0.0% 0	0.0% 0	0.0% 0	0.0% 0
Femur	0.0% 0	0.0% 0	0.2% 1	0.0% 0	0.0% 0	99.8% 519	0.0% 0	0.0% 0	0.0% 0
Lips	0.0% 0	0.0% 0	0.0% 0	0.0% 0	0.0% 0	0.0% 0	99.8% 525	0.0% 0	0.3% 1
LVOT	1.0% 3	0.0% 0	0.0% 0	0.0% 0	0.0% 0	0.0% 0	0.0% 0	95.8% 319	0.3% 1
RVOT	6.4% 19	0.0% 0	0.0% 0	0.0% 0	0.0% 0	0.0% 0	0.2% 1	1.8% 6	94.9% 281

Fig. 15: Class confusion metrics for 2D ultrasound standard plane classification. Upper row left: the class confusion matrix without shadow confidence maps. Upper row right: the class confusion matrix with the shadow confidence maps generated by the baseline. Lower row left: the class confusion matrix with shadow confidence maps obtained by the proposed method. Lower row right: the class confusion matrix with the shadow confidence maps produced by the proposed+AG method.